Journal of Nanobiotechnology

RESEARCH

Open Access

Bionic gene delivery system activates tumor autophagy and immunosuppressive niche to sensitize anti-PD-1 treatment against STK11-mutated lung adenocarcinoma

Zhongquan Song[1†], Qikai Wang[2†], Hongjie Xiong[3], Jiang Xiao[3], Zihan Zhou[1], Tianxiang Li[1], Qian Sun[1], Liping Qiu[1], Yue Tan[1], Xiaohui Liu[3*], Hui Jiang[3*], Shuhua Han[1*] and Xuemei Wang[3*]

Abstract

Clinical data have shown that Serine/Threonine Kinase 11 (STK11) mutation may be associated with an immunosuppressive tumor microenvironment (ITEM) and poor prognosis and failure of anti-PD-1 (αPD1) treatment in non-small cell lung cancer (NSCLC). To explore the potential of restoring STK11 protein in immunotherapy, a bionic gene delivery system was prepared by coating the STK11-encoded DNA-cationic polymer complex core with the tumor cell membrane, termed STK11@PPCM. STK11@PPCM could specifically bind with NSCLC cells and achieve precise delivery of STK11-encoded DNA. The released DNA effectively restored the STK11 protein expression, consequently reactivating autophagy and immunogenic cell death (ICD) in cancer cells. The liberated damage-associated molecular patterns (DAMPs) and autophagosome induced dendritic cells (DCs) maturation, which in turn enhanced CD8+T cell infiltration, M1 macrophage polarization, and proinflammatory factor expression, thereby reversing the ITEM. Moreover, STK11@PPCM was also found to improve the sensitivity of cancer cells to αPD1 by increasing the expression of PD-L1, which was confirmed in STK11-mutated NSCLC cell xenografted mouse models, constructed by CRISPR-Cas9 knockout technology. This work demonstrated for the first time that restoration of functional STK11 can effectively reverse ITME and boost αPD1 efficacy in NSCLC, offering a new therapeutic approach for STK11-mutated lung adenocarcinoma in clinic.

Keywords Lung adenocarcinoma, STK11 gene therapy, Anti-PD-1 treatment, Autophagy, Tumor immune microenvironment, Bionic drug delivery

[†]Zhongquan Song and Qikai Wang co-first authors.

*Correspondence:
Xiaohui Liu
101013182@seu.edu.cn
Hui Jiang
sungi@seu.edu.cn
Shuhua Han
hanshuhua0922@126.com
Xuemei Wang
xuewang@seu.edu.cn

Full list of author information is available at the end of the article

Graphical abstract

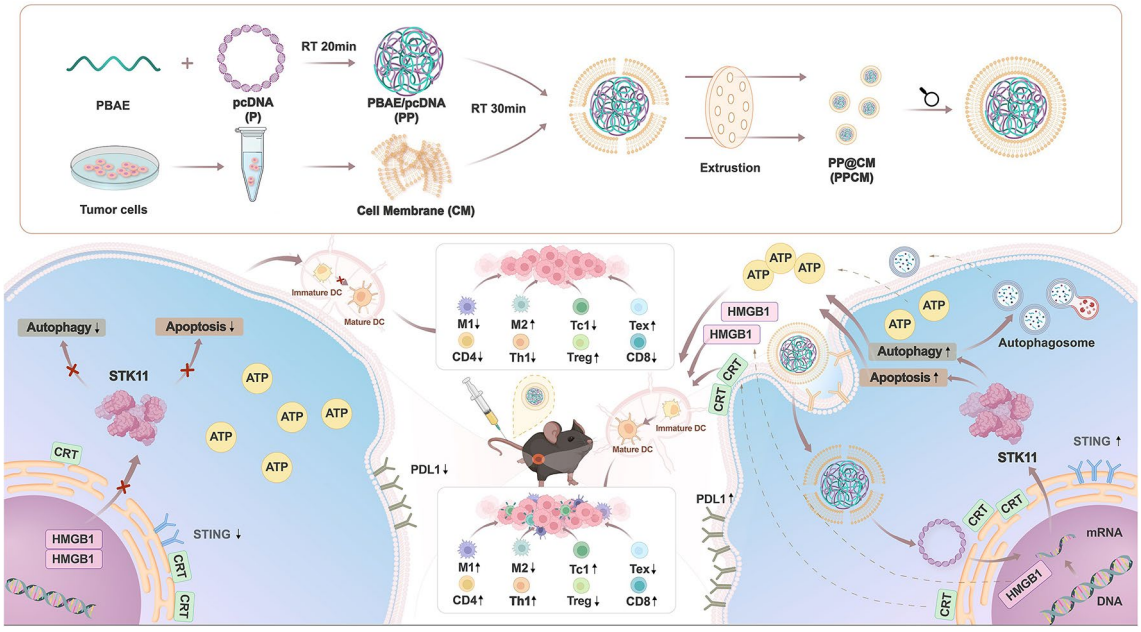

Introduction

Lung cancer still occupies the top of the cancer spectrum in terms of new cases and deaths, according to malignant tumor disease burden in 2022 [1]. The emergence of immune checkpoint inhibitors (ICIs) represented by programmed cell death-1 (PD-1) or programmed cell death-Ligand 1 (PD-L1) antibodies has greatly improved the prognosis of patients [2]. However, it has been demonstrated that less than 30% of patients with NSCLC benefited from ICIs, and 20–44% of patients showed resistance to ICIs [3]. It was imminent to identify potential factors affecting the efficacy of immunotherapy.

STK11 is a tumor suppressor gene, which affects cellular processes such as cellular metabolism, cell polarization, regulation of apoptosis, and DNA damage response [4]. Somatic loss-of-function mutation of STK11 occurs in multiple cancer types, especially in lung adenocarcinomas [5], and can lead to the deletion of the encoded protein [6]. Recent clinical and preclinical studies have revealed that STK11 mutation was an important cause of resistance to ICIs [7–11]. The main reason is that STK11 mutation can directly shape a "cold" immune microenvironment [12]. The STK11 mutation could contribute to the accumulation of suppressive immune cells in the tumor site, such as regulatory T cells (Treg), neutrophils, exhaustion T cells (Tex), and M2 macrophages (M2), and the decrease of CD8 + T cells infiltration and stimulator of interferon genes (STING) expression [13–16]. Meanwhile, the mutation was also reported to down-regulate autophagy and apoptosis of cancer cells [17–19]. Tumor autophagy could promote ICD and cause the release of DAMPs and autophagosomes [20, 21]. The liberated DAMPS (e.g. ATP, high-mobility group box 1 (HMGB1), and calreticulin (CRT)) and tumor antigens loaded in autophagosomes can induce DCs maturation and activate anti-tumor immunity [22–24]. Moreover, the down-regulated PD-L1 expression induced by STK11 mutation further impaired the efficacy of ICIs [13–16].

So far, some measures have been taken to enhance the sensitivity of STK11 mutant lung cancer to ICIs, such as metformin [25, 26], PD-1/PD-L1 inhibitors in combination with chemotherapy and/or cytotoxic T lymphocyte-associated antigen-4 (CTLA-4) inhibitors [27], inhibitor of STAT3 [10] and so on. However, these treatments demonstrated more severe toxicity or transiently activated anti-tumor immunity. Nevertheless, it has not been reported whether restoration of STK11 expression in STK11-mutated cells could reverse the ITME and enhance antitumor immunity by inducing reactivation of autophagy and ICD to improve the efficacy of ICIs.

It is known that nucleic acids, such as DNA, mRNA, siRNA, or miRNA, have been widely explored to modulate protein expression and multiple immune processes and play an important role in enhancing anti-tumor immunity. So, restoration of STK11 expression by gene therapy is expected to sensitize STK11-mutated cells to the αPD1. Recently, gene therapies combined with nanomaterials have broadened the therapeutic and biomedical applications of these nucleic acids [28–30]. Poly (β-amino) esters (PBAEs) are a class of biodegradable

cationic polymers with the advantages of low cytotoxicity and high transfection efficiency [31], which makes them particularly suitable for the delivery of genes, proteins, and peptides [32–34]; however, the lack of targeting and low bioavailability limit their application. To our delight, cell membranes (CMs)-coated nanoparticles have been proposed as vesicles for gene delivery [35, 36], which can prolong blood circulation time, increase biocompatibility, and improve homotypic tumor-targeting effects. So far, CMs from tumor cells have been investigated for the preparation of biomimetic nanoparticles and have become the most widely studied biofilms for cancer therapy [37].

Given the above considerations, we developed a bionic nanoplatform (STK11@PPCM), which was composed of PBAE with the ability to complex the plasmid DNA (pcDNA) encoding STK11 and a layer of tumor cell membrane (Scheme 1). As shown in Scheme 1, once reaching the tumor site, STK11@PPCM could selectively target cancer cells and enhance cellular uptake based on a membrane-mediated homologous targeting strategy. After internalization, the "proton sponge" effect of PBAE enabled the rupture of STK11@PPCM and effectively released plasmid to restore the STK11 expression. Consequently, apoptosis and autophagy were initiated. Multiple DAMPs and autophagic vesicles were released to promote the activation of DCs, cytotoxic T lymphocytes, M1 macrophages, and secretion of proinflammatory factors, which eventually established a "hot" immune microenvironment to reinforce the αPD1 efficacy. On the other hand, the upregulated PD-L1 expression further boosted the efficacy of αPD1. This work demonstrated significant antitumor effects of the combination of STK11-encoded bionic DNA nanodrug and αPD1, providing a paradigm for the management of STK11-mutated lung adenocarcinoma in the clinic.

Results

STK11 mutation reduces the benefit of ICIs in patients with LUAD

To evaluate the effect of STK11 mutation on STK11 protein expression and the prognosis of patients with LUAD, we carried out a bioinformatic analysis. Firstly, we analyzed the relationship between STK11 mutation status and STK11 expression in the training dataset GSE72094 [38] and the validation dataset GSE193895 [39]. STK11 differential expression analysis showed that the mutant group had lower protein expression compared to the wild group in GSE72094 (Fig. 1A), and the same result was also obtained in GSE193895 (Fig. 1B). Next, we analyzed the relationship between STK11 expression level and the overall prognosis in GSE30219 [40] and GSE31210 [41, 42] from KM-plotter database. Survival analysis showed that the relevant low-expression group had a poor overall survival (OS) compared with the high-expression group (Fig. 1C). Likewise, an obvious difference could be identified in GSE31210 (Fig. 1D). At last, we further evaluated the relationship between STK11 mutation status and the efficacy of ICIs. According to OS, we found that the STK11 wild group benefited more from immunotherapy compared to the mutant group in GSE161537 [43, 44] (Fig. 1E). At the same time, we can observe that the STK11 wild group was able to achieve a relatively higher progression-free survival (PFS) from immunotherapy compared to the mutant group in GSE135222 [45, 46], although there were no statistically significant differences (Fig. 1F).

STK11 mutation induces a "cold" immune microenvironment in LUAD

To clarify the reasons for the poor prognosis of patients with STK11-mutated LUAD, we further evaluated the immune infiltration at the transcriptome level and the single-cell level in STK11-mutated LUAD. At the transcriptome level, through the TIMEDB online database, we found that there was less infiltration of immune-activated cells, such as CD8 + T cells, DCs, etc., in patients with STK11 mutation, compared to the wild group (Fig. 1G). Similarly, we found that the STK11 mutant group had fewer infiltration of immune-activated cells and more infiltration of immunosuppressive cells, compared to the wild group in dataset GSE193895 by the CIBERSORT algorithm (Fig. S1A). Meanwhile, the STK11 mutation group had relatively lower immunity scores, as evidenced by lower ESTIMATE Score, lower Immune Score, and lower Stromal Score in dataset GSE193895 through the ESTIMATE algorithm (Fig. S1B). Next, we have also evaluated the effect of STK11 mutation on immune escape ability and immune checkpoints gene expression. By analyzing the dataset GSE193895, we found that the mutant group had a higher TIDE score, lower expression of immune checkpoint genes, and higher CP_IPS score, compared to the wild group (Fig.1H and Figs. S1C-D). At the single-cell level, we further confirmed the above results by cellular fractionation and quantitative analysis of sequenced samples from the dataset GSE231742 [15] (Figs. 1I-K). Identical observations were also confirmed by IHC of tissue sections from patients with STK11 mutated or unmutated LUAD (Fig. S2).

Preparation and characterization of STK11@PPCM for gene delivery to tumor cells

To explore whether restoring STK11 expression could enhance antitumor immunity in vivo or in vitro, we first constructed an STK11-deficient stably-transformed cell line (LLC ^{KO}) on LLC cells using CRISPR-dual gRNA/Cas9 technology (Figs. S3-S4). Then, we constructed

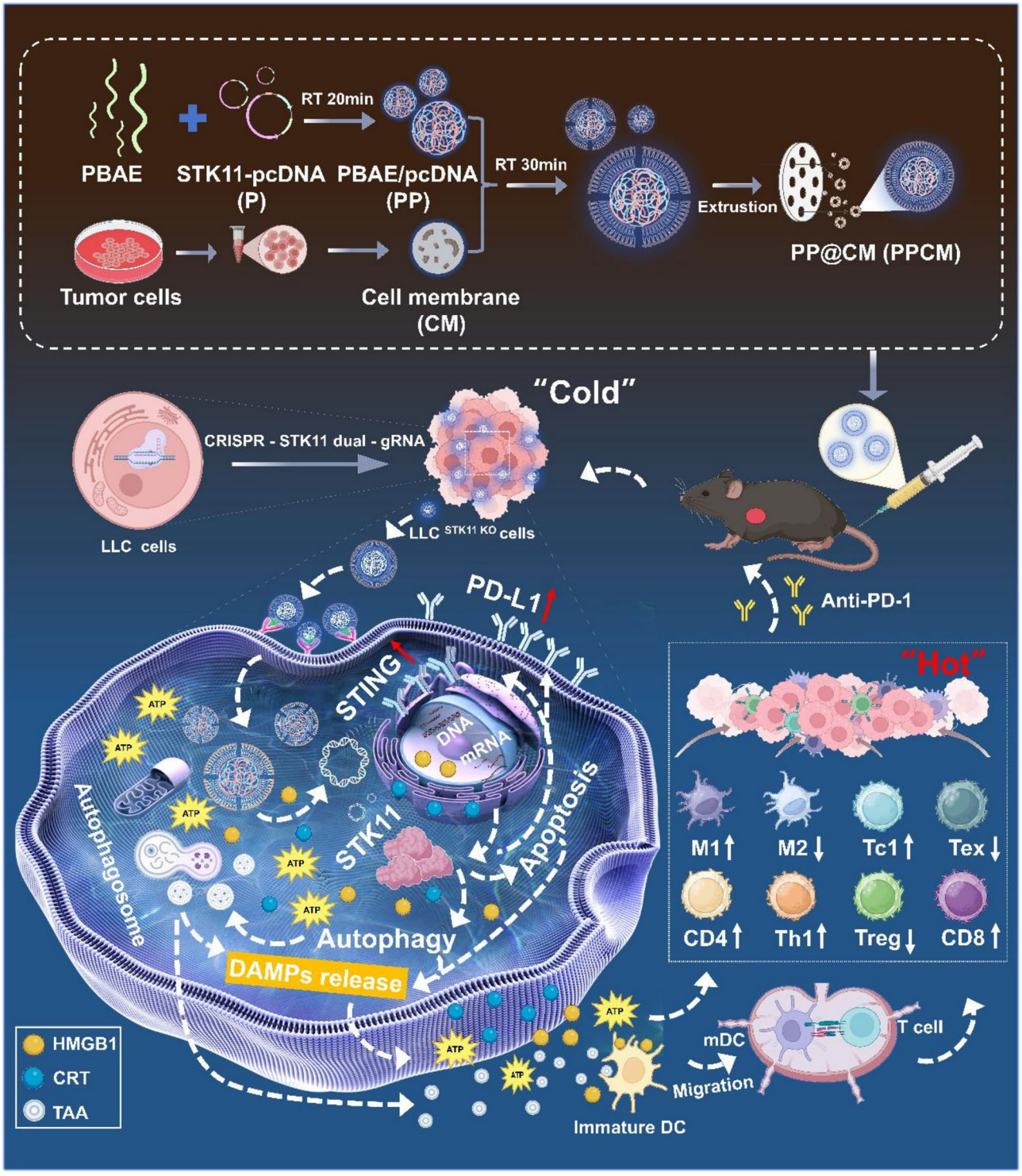

Scheme 1 Schematic illustration of STK11@PPCM reversing the immune microenvironment and enhancing anti-tumor immunity. M1, Type I macrophages; M2, Type II macrophages; Tc1, Type I CD8 + cytotoxic T cell; Tex, exhaustion T cell; CD4, CD4 + T cell; Th1, Type I T helper cell; Treg, regulatory T cells; CD8, CD8 + T cell

a new nucleic acid delivery platform (STK11@PPCM) composed of cationic polymers PBAE and the anionic plasmid encoding STK11, encapsulated by tumor cell membrane to actively target tumor lesions (Fig. 2A). PBAE was initially prepared in a two-step process [47, 48] (Figs. S5-S6) and used to complex plasmid DNA to form the PBAE/DNA complex (termed PP) by self-assembly method. Meanwhile, the tumor cells membrane

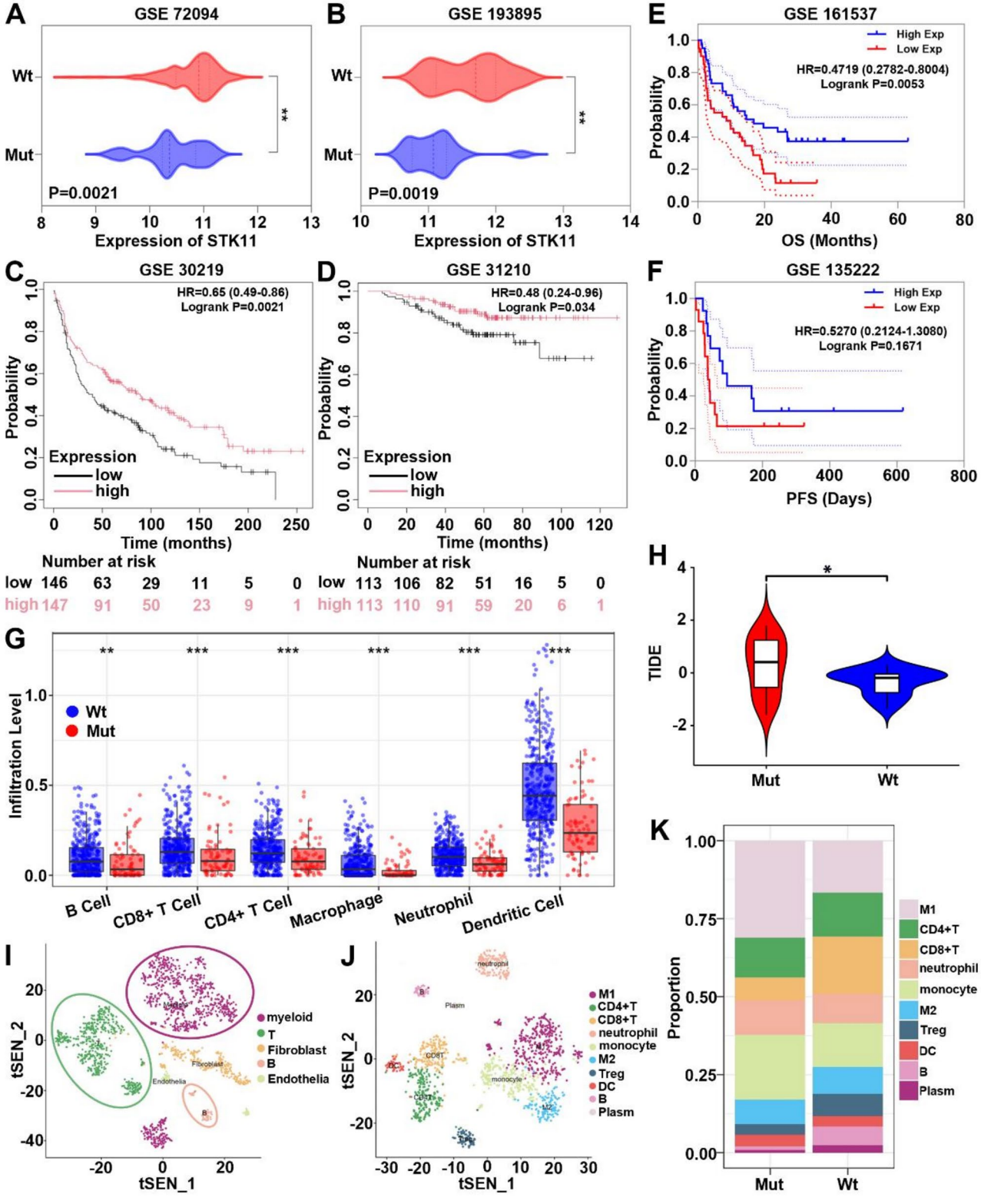

Fig. 1 (See legend on next page.)

(See figure on previous page.)

Fig. 1 Prognosis and immune infiltration induced by STK11 mutation in lung adenocarcinoma. (**A**) Relationship between STK11 mutation status and STK11 expression in the training dataset GSE72094 (*N* = 442). (**B**) Relationship between STK11 mutation status and STK11 expression in the validation dataset GSE193895 (*N* = 35). (**C**) Relationship between STK11 expression and prognosis of patients with lung adenocarcinoma in the training dataset GSE30219 (*N* = 307). (**D**) Relationship between STK11 expression and prognosis of patients with lung adenocarcinoma in the validation dataset GSE31210 (*N* = 246). (**E**) Relationship between STK11 expression (high and low expression represented wild type and mutant type in the graph) and overall survival (OS) of patients treated with ICIs in the dataset GSE161537 (*N* = 82). (**F**) Relationship between STK11 expression (high and low expression represented wild type and mutant type in the graph) and progression-free survival (PFS) of patients treated with ICIs in the dataset GSE135222 (*N* = 27). (**G**) Relationship between STK11 mutation status and level of immune infiltration in the TIMEDB. (**H**) Relationship between STK11 mutation status and tumor immune escape ability in the dataset GSE193895 (TIDE score reflects the potential for tumor immune evasion, and higher TIDE score is associated with poor outcome). (**I**) Single-cell RNA sequencing gene expression clusters in the dimensional reduction projection (UMAP) in the database GSE231742, which shows the different identified cell populations. Labels have been added based on the expression of marker genes. T cells, B cells, and myeloid cells were highlighted in different colored circles. (**J**) Subclusters of all immune cells in the UMAP diagram in the database GSE231742. (**K**) Quantitative analysis of infiltration of all immune cell subtypes in the database GSE231742. Statistical significance: $^{*}P < 0.05$, $^{**}P < 0.01$, $^{***}P < 0.001$

was extracted and further coated on PP to form the PP@CM complex (termed PPCM) by ultrasound and extrusion [49, 50].

The morphology and size distribution of obtained PP and PPCM were characterized by transmission electron microscopy (TEM). The typical spherical structure of PP and PPCM could be observed (Fig. 2B and Fig. S7), and the size of PP was 25.32 ± 1.04 nm (Fig. 2C). After coating with the cell membrane, a thin membrane structure can be seen on the surface of PP to produce slightly larger particle (A549-PPCM, 75.54 ± 4.14 nm; LLC ^{KO}-PPCM, 83.77 ± 3.89 nm) (Fig. 2C). The zeta-potential results showed that the PP had a surface charge of approximately 19.9 mV, and the surface charge of PPCM decreased to around − 6.9 mV (A549-PPCM) and − 8.5 mV (LLC ^{KO}-PPCM) (Fig. 2D). Meanwhile, after 8 days of storage at 4 °C, the mean particle diameter of the PPCM did not change significantly (Fig. S8). The result above suggested the stability of the structure of the PPCM to some extent.

The agarose gel electrophoresis was used to assess the interaction of PBAE and DNA. It was found that plasmid DNA was adequately bound at the PBAE/DNA mass ratios of 30, 60, and 90 (Fig. 2E), and the mass ratio of 90 was used in this study. Meanwhile, we evaluated the serum stability of the STK11@PPCM and the ability of the nanocomplexes to protect and release DNA. It was found that STK11@PPCM had better serum stability and ability of DNA protection and release, compared to STK11@PP (Fig. S9). In addition, the binding and releasing ability of PBAE on DNA was further confirmed by kinetic analysis (Fig. S10). As shown in Fig. S10A, compared to naked Cy5-DNA, the free DNA content in solution decreased at an accelerated rate when the DNA was co-incubated with PBAE, and the free DNA was almost close to 0 when the incubation reached 30 min. Due to the protonation of the tertiary amine group in PBAE in a weakly acidic environment, DNA release from the nanocomplex gradually accelerated and ultimately entered a plateau phase in a weakly acidic medium. On the contrary, no significant change was detected in the neutral environment (Fig. S10B).

To confirm whether the membrane proteins were still reserved after extrusion, we performed SDS-PAGE analysis of total proteins from extracted cell membranes and found that protein bands from PPCM were almost identical to CM and cells in A549 and LLC ^{KO} (Fig. S11). Next, the toxicity of STK11@PPCM to A549 and LLC ^{KO} cells was evaluated by CCK8 assays. The CCK8 assays showed that the PPCM did not have obvious cytotoxicity in the tested range of doses (Fig. 2F). However, the PP complexes exhibited toxic responses in a dose-dependent manner (Fig. 2F). Moreover, A549 and LLC ^{KO} cells were pretreated with different inhibitors to investigate STK11@PP and STK11@PPCM internalization pathway. We found that β-CD could remarkably inhibit the uptake of PP in two cells; however, PPCM uptake was not affected. And, neither promethazine nor amiloride could inhibit the internalization of PP and PPCM in two cells (Figs. 2G-H and Figs. S12-S13). Based on this, it was reasonable to consider that the endocytosis pathway of PPCM was independent of the conventional endocytosis pathway and may though a receptor-mediated pathway [51].

Transfection efficacy of PPCM

To evaluate the transfection efficiency of PPCM, the transfection of plasmid encoding enhanced green fluorescence protein (EGFP) was carried out in A549 and LLC ^{KO} cells. As shown in Fig. 2I, PP and PPCM exhibited excellent transfection capability, and quantitative analysis indicated that the proportion of EGFP-positive cells for PP and PPCM was close to 40% and 30% in A549 cells (Fig. 2J). It was amazing the proportion of EGFP-positive cells for PP and PPCM was close to 50% and 40% in LLC ^{KO} cells (Fig. 2J). At the same time, we found that PP and PPCM have higher transfection efficacy compared to the transfection reagents currently available on the market, including PEI25K and Lipofectamine 2000, although the PPCM showed slightly declined transfection efficiency, compared to PP (Fig. 2I-J). This may be explained by two hypotheses [52]. First, cellular uptake of PPCM may be reduced. Compared to the negative surface charges of PPCM, the positive charges of PP are more favorable for

cellular uptake. The second hypothesis was that PPCM has a reduced lysosomal escape capacity, due to the interference with the proton buffering effect of PBAE by the tumor cell membrane.

To test the first hypothesis, Cy5-labeled plasmid DNA was used to prepare the PP and PPCM. The cellular uptake of the PPCM tended to increase, compared to PP in two cells (Fig. S14A). Quantitative analysis by FCM further confirmed that PPCM had higher cellular uptake in A549 and LLC ^{KO} cells (Figs. S14B-C). According to the result, the cellular uptake efficiency could not account for the lower transfection efficiency of PPCM. To further explore the second hypothesis, we evaluated the lysosomal escape ability of PP and PPCM in A549 and LLC ^{KO} cells. PP showed red signals in the absence or presence of chloroquine in two cell lines (Fig. S14D). No red fluorescence was observed in the absence of chloroquine, while the treatment group with PPCM showed more red fluorescence in the presence of chloroquine (Fig. S14D). Therefore, the reduced transfection efficiency of PPCM might be explained through inefficient endosomal escape [52].

Effect of restoring STK11 expression on cell viability, invasion, and migration

To investigate whether functions of STK11 can be restored by our constructed DNA delivery system, we first constructed the STK11 plasmid DNA and performed extensive extractions (Figs. S15-S17, Table S1), and then, STK11 expression was tested via WB and qRT-PCR when cells were treated with PBS, naked STK11-DNA (P), STK11@PP, or STK11@PPCM for 48 h. As shown in Figs. 3A-B and Fig. S18A, the STK11 plasmid DNA delivery platform could increase STK11 expression at the level of transcription and translation. At the same time, the PP group has relatively higher STK11 expression compared to the PPCM group, which can be correlated with the different transfection efficiency shown in Sect. 2.4 (Figs. 3A-B and Fig. S18A). In addition, we also explored the effect of restored STK11 expression on cell viability and found that cell viability decreased in PP and PPCM groups after STK11 expression was restored (Fig. 3C).

Based on the above observations, we explored whether the restoration of STK11 expression could inhibit cell proliferation, invasion, and migration. The transwell assays were performed in vitro to assess the capacity of invasion and migration of A549 and LLC ^{KO} cells treated with PBS, naked STK11 DNA, STK11@PP, or STK11@PPCM for 48 h. The results demonstrated that the restoration of STK11 expression could effectively reduce the number of cells of invasion and migration of A549 and LLC ^{KO} cells (Figs. 3D, H). The in vitro wound healing assays also confirmed the above results (Figs. 3E-F, I). At the same time, the colony formation study demonstrated that the increase of STK11 had an antiproliferation effect on cells (Fig. 3G). Hence, our findings further confirmed that loss of STK11 promoted invasion and migration of cells, and reintroducing the functional STK11 protein could effectively alleviate the tendency.

Restoration of STK11 protein function induced autophagy, apoptosis, and ICD

As noted in the 2.5 section, when the A549 and LLC ^{KO} cells were treated with PBS, naked DNA, PP, or PPCM for 48 h, PP and PPCM groups demonstrated significant proliferation inhibition, while no inhibition of proliferation was seen in the control and naked DNA groups. To explore the potential mechanisms by which STK11 restoration promoted tumor cell death, we performed a transcriptomic analysis between STK11 mutation type and STK11 wild type in human samples in the dataset GSE72094. This step aimed to identify genes that were significantly differentially expressed in the two groups by plotting the volcano map. As the results demonstrated, the STK11 mutation group has 426 genes were significantly down-regulated and 327 genes were up-regulated (Fig. 4A). The functional enrichment of down-regulated genes was further analyzed, and the GO analysis demonstrated that the down-regulated genes were linked to apoptotic process and autophagy (Fig. 4B). Thus, it is apparent that autophagy and apoptosis were down-regulated in the STK11 mutant group, and autophagy and apoptosis were reactivated when STK11 function was restored, thereby inhibiting cell proliferation [17–19]. The induction of autophagy and apoptosis could also promote the release of DAMPs [20, 21], thus triggering the ICD and enhancing antitumor immune response [21]. Hence, it is reasonable that the restoration of STK11 protein function may trigger ICD by the release of DAMPs caused by reactivated apoptosis and autophagy (Fig. 4C).

To confirm the induction of autophagy, A549 and LLC ^{KO} cells transfected by Lentivirus (mRFP-EGFP-Pruo) CMV-LC3B were exposed to either PBS, naked STK11 DNA, STK11@PP or STK11@PPCM for 48 h. As shown in Fig. 4D and Fig. S19, there was more autophagosome formation in the tumor cells treated with PP or PPCM than in those treated with naked STK11 DNA or PBS, suggesting that STK11 nanocomplex can effectively induce autophagy. Meanwhile, the presence of autophagy induced by STK11 activation can be validated at molecular levels. The WB was used to test the expression of autophagy signature proteins LC3-I/II and p62. As a result, it can be found that LC3-I did not change in the four groups, while LC3-II was significantly upregulated in the PP and PPCM groups compared to the others (Fig. 4E and Fig. S18A). Besides, it demonstrated the same trend for p62 protein, suggesting that STK11

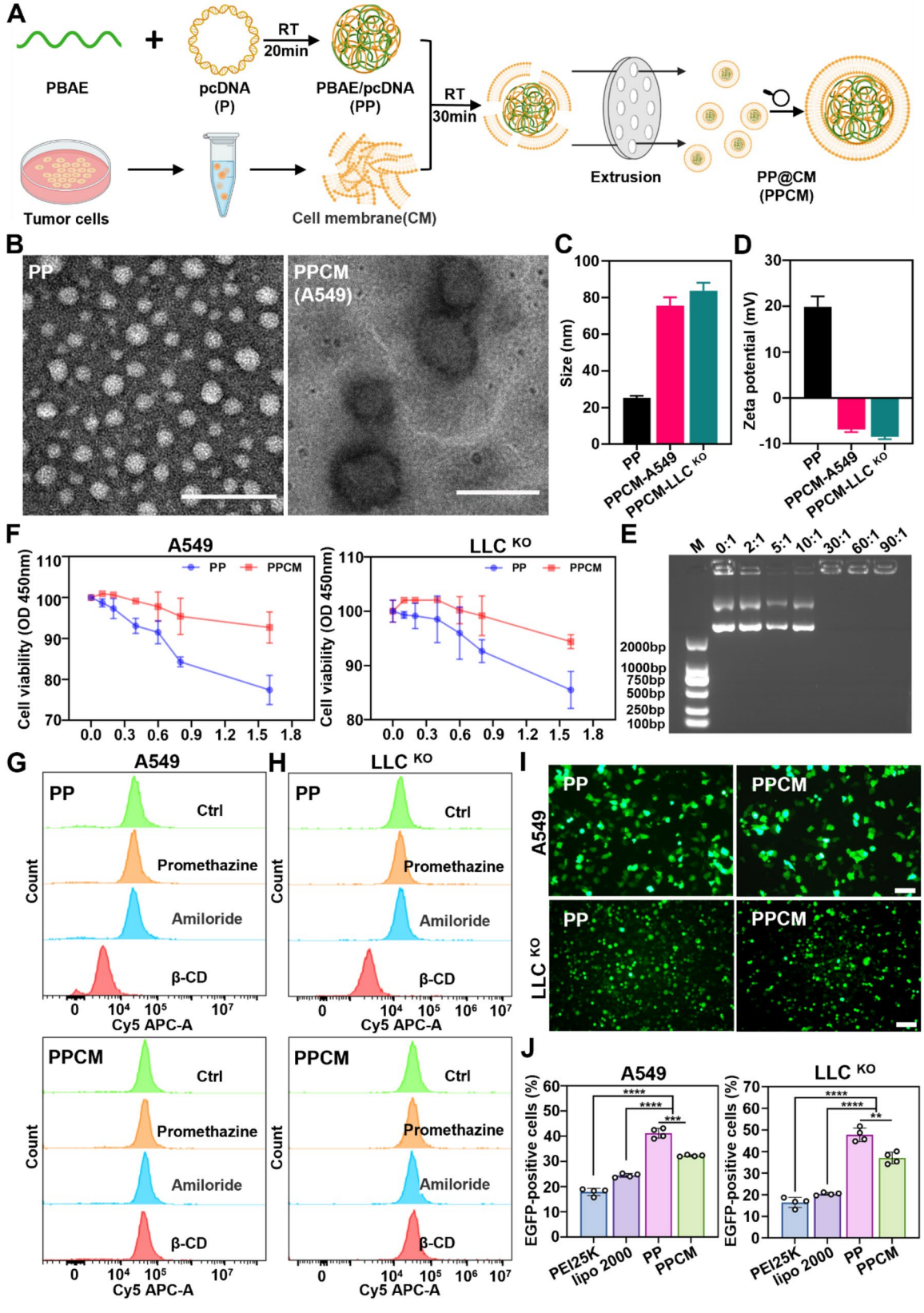

Fig. 2 (See legend on next page.)

(See figure on previous page.)

Fig. 2 Construction and characterization of STK11@PPCM. (**A**) Flowchart for the construction of STK11@PPCM. (**B**) TEM image of PP and A549-PPCM. Scale bar, 100 nm. (**C**) The size distribution of PP, A549-PPCM, and LLC ^{KO}-PPCM was detected by TEM. The data represented means ± SD ($n = 3$). (**D**) Zeta potential analysis of PP, A549-PPCM, and LLC ^{KO}-PPCM. The data represented means ± SD ($n = 3$). (**E**) Plasmid DNA gel imaging for different ratios of PBAE/DNA. (**F**) Toxicity analysis of PP and PPCM on A549 and LLC ^{KO} cells by CCK8 assays. The data represented means ± SD ($n = 5$). (**G**) Investigation of cellular uptake mechanism of PP and PPCM prepared by Cy5-labeled plasmid in A549 by FCM. (**H**) Investigation of cellular uptake mechanism of PP and PPCM prepared by Cy5-labeled plasmid in LLC ^{KO} by FCM. (**I**) Fluorescence images of A549 and LLC ^{KO} cells transfected with PBAE/EGFP or PBAE/EGFP/CM. Scale bar, 100 μm. (**J**) Quantitative analysis of EGFP-positive cells from A549 cells and LLC ^{KO} cells transfected with PP, PPCM, PEI25K, and Lipo2000 by FCM. The data represented means ± SD ($n = 4$) and analyzed by a one-way ANOVA with a Tukey post-hoc test. Statistical significance: $^{**}P < 0.01$, $^{***}P < 0.001$, $^{****}P < 0.0001$ versus Ctrl

nanocomplex induced autophagy formation (Fig. 4E and Fig. S18A).

Next, we explored the apoptosis induced by restoration of STK11 expression in A549 and LLC ^{KO} cells. It showed a higher ratio of apoptosis in PP (18.46%) and PPCM (15.38%) groups compared to the naked STK11 DNA (2.93%) or the PBS (2.68%) in A549 cells (Fig. 4F), and the same result can be observed in LLC ^{KO} cell (Fig. 4G). Meanwhile, the TUNEL assays also confirmed that the restoration of STK11 could activate the apoptotic process (Fig. S20).

The induction of autophagy and apoptosis could promote the release of DAMPs [20, 21], triggering the ICD. We also explored the possibility of the STK11 nanocomplex-induced DAMPs release to activate ICD. Herein, hallmark markers of ICD, CRT, HMGB1, and ATP, were measured. The CRT was determined by immunofluorescence and a higher red fluorescence intensity was shown in PP and PPCM groups in two cell lines (Fig. 4H). Likewise, compared to the naked STK11 DNA and PBS group, there was a remarkable increase in HMGB1 and ATP secretion for A549 and LLC ^{KO} cells treated with PP and PPCM (Figs. 4I-J). In addition, the loss of STK11 protein function led to down-regulation of STING and PD-L1 expression [14], here we further assessed the effect of restoration of STK11 expression on STING and PD-L1 expression. As demonstrated in Figs. S18A-C, the restoration of STK11 function significantly increased the expression of STING and PD-L1. Based on these observations, it was obvious that the restoration of STK11 function promoted ICD and the expression of immunotherapy-positive genes, which provided a theoretical basis for the assessment of anti-tumor immunity in vivo.

The "cold" immune microenvironment was reversed by STK11@PPCM in the mouse model

We have demonstrated that the restoration of STK11 function can activate ICD in vitro. However, it was still not clear whether restoration of STK11 function can reverse the immunosuppressive microenvironment in vivo and enhanced the anti-tumor immune response. Firstly, we constructed a subcutaneous LLC ^{KO} tumor model using C57BL/6 mice and measured the biodistribution of PPCM. When the tumor volume reached 60–80 mm^3, the tumor-bearing mice were randomly divided into 4 groups, which were injected respectively with 100 μl solution containing PBS, naked EGFP DNA, PBAE/EGFP, and PBAE/EGFP/CM via tail veins. After 72 h, major organs (i.e., heart, liver, spleen, lung, and kidney) and tumors were isolated and imaged. Mice treated with PPCM showed relatively higher fluorescence in tumors, compared to PP (Fig. S21), suggesting that PPCM has excellent tumor-targeting properties.

Next, we evaluated the effect of STK11@PPCM on the tumor immune microenvironment and anti-tumor immune response using LLC ^{KO} tumor-bearing mice. When the average tumor volume reached 60–80 mm^3, the mice were randomly divided into 4 groups (PBS, naked STK11 DNA, STK11@PP, and STK11@PPCM) and treated at a plasmid dose of 25 μg per mouse via tail vein injection at day 10, 13, and 16 after tumor cell implantation (Fig. 5A). To exclude the effect of ICIs themselves on the tumor microenvironment and PPCM, we added two groups of mice and treated respectively with αPD1 and αPD1 + STK11@PPCM (αPD1 dose of 100 μg in 100 μl saline per mouse) at day 11, 14, and 17. At day 19 (2 days after the last injection), all mice were euthanized and the tumors and lymph nodes were harvested to assess the number and phenotype of immune cells and changes in secreted cytokines (Fig. 5A). The "cold" tumors were distinguished from the "hot" tumors mainly by the spatial distribution of immune cells [53] (Fig. 5B). Among them, DCs, CD4 + T cells, CD8 + T cells and macrophage played an important role in remodeling the tumor immune microenvironment [54]. Here, we focused on evaluating the effect of STK11@PPCM on DCs, CD4 + T cells, CD8 + T cells, and macrophage infiltration.

We first analyzed various stimulatory molecules expressed on lymph node–resident DCs (LNDCs) after treatment with STK11@PPCM. The infiltration of CD11c + MHC-II + cells, CD80 + CD86 + cells, CD11c + CD8 + cells (cDC1), and CD11c + CD11b + cells (cDC2) significantly increased after three cycles of treatment (Figs. 5C, F and Figs. S22-S23). DCs activate anti-tumor immune response primarily by presenting antigen to T cells, activating T cells, and initiating effector T cell response against tumor-associated antigen (TAA). The percentage of CD3 + CD4 + T cells and CD4 + IFNγ+ T cells within the tumor was increased (Fig. 5G and

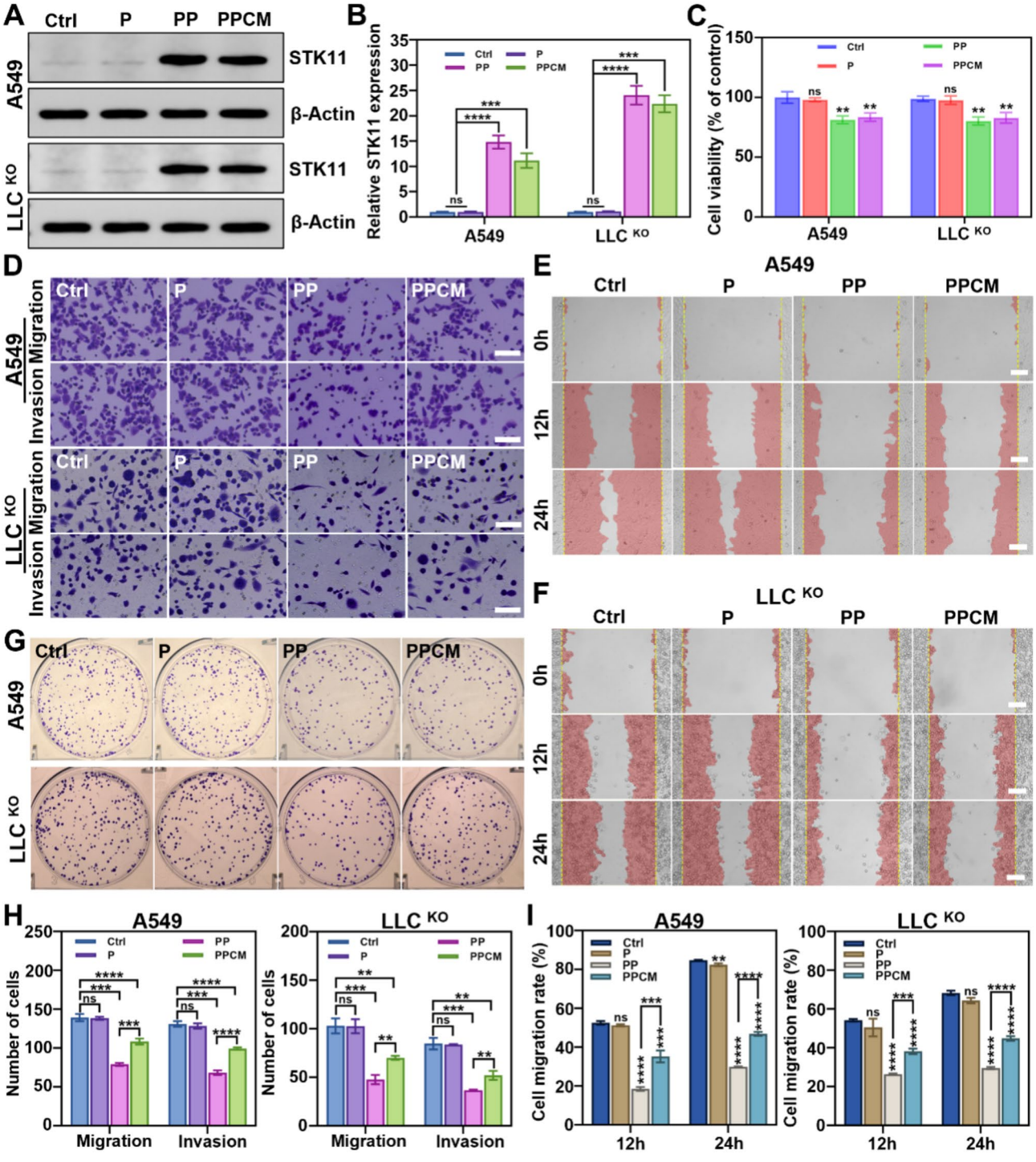

Fig. 3 STK11 expression induced by STK11@PPCM and effects on cell viability. (**A**) Western blot analysis of STK11 expression in A549 and LLC ^{KO} cells after indicated treatments for 48 h. (**B**) RT-PCR for STK11 in A549 and LLC ^{KO} cells after indicated treatments for 48 h. Cells without treatment (Ctrl) served as the background. The data represented means ± SD ($n = 3$). (**C**) Cell viability of A549 and LLC ^{KO} cells after indicated treatments for 48 h. Data are presented as means ± SD ($n = 5$). (**D**) Images of invasion and migration of A549 and LLC ^{KO} cells after indicated treatments for 48 h by transwell assays. Scale bar, 100 μm. (**E** and **F**) Images of A549 and LLC ^{KO} cells after indicated treatments for 48 h by wound healing assays (incubation time: 0, 12, and 24 h). Red cells represent migrating cells. Yellow lines represent the borderlines. Scale bar, 100 μm. (**G**) Colony formation assays of A549 and LLC ^{KO} cells after indicated treatments for 48 h. (**H**) Quantitative analysis of cell number for invasion and migration of A549 and LLC ^{KO} cells in part D. The data represented means ± SD ($n = 3$). (**I**) Quantitative analysis of the in vitro wound healing assays of A549 and LLC ^{KO} cells in parts E and F. The data represented means ± SD ($n = 3$). Data was analyzed by a one-way ANOVA with a Tukey post-hoc test. Statistical significance: $^{**}P < 0.01$, $^{***}P < 0.001$, $^{****}P < 0.0001$ versus Ctrl

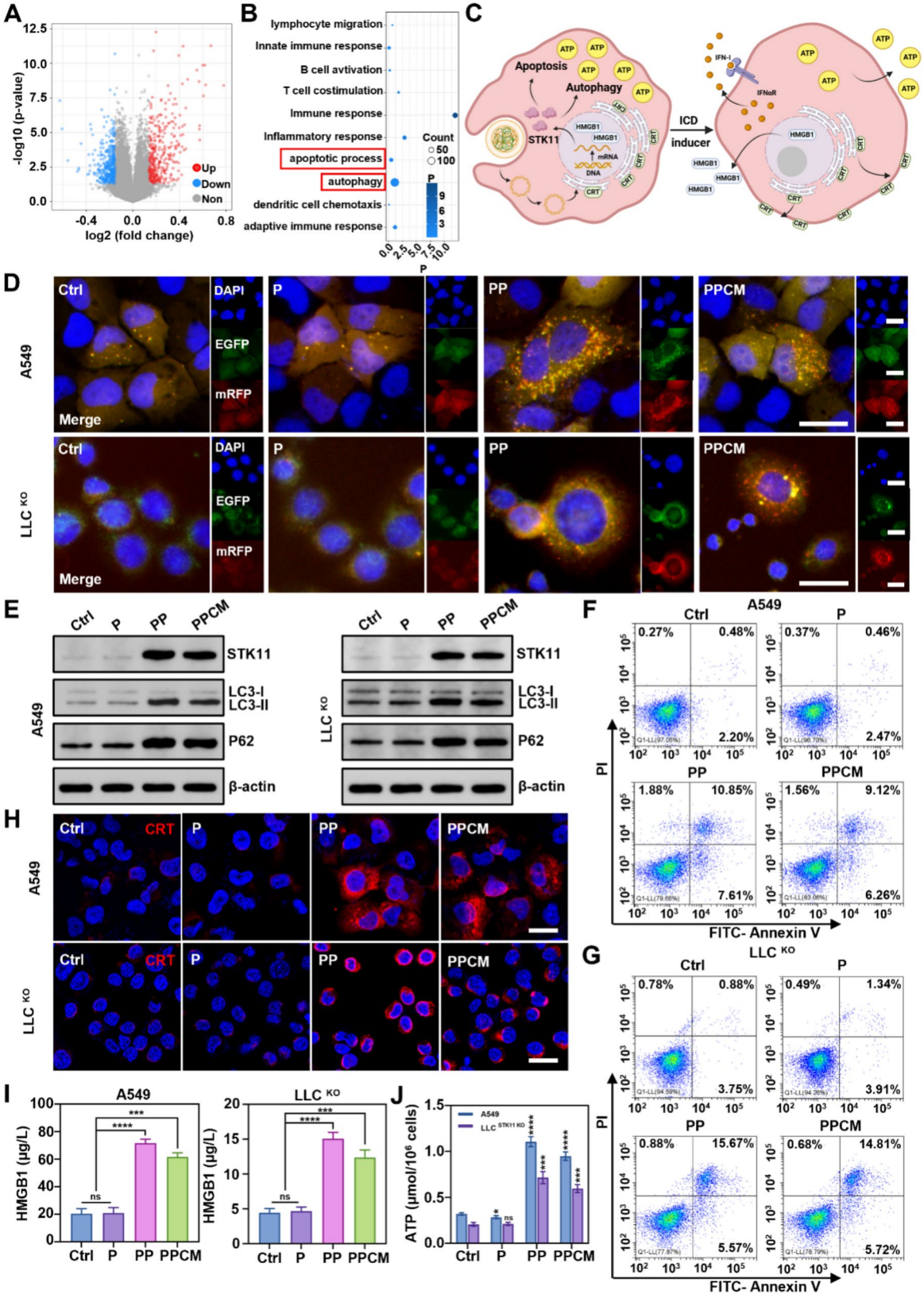

Fig. 4 (See legend on next page.)

(See figure on previous page.)

Fig. 4 STK11 nanocomplexes induced ICD of tumor cells in vitro. (**A**) Volcano plot of differentially expressed genes in STK11 mutation (before STK11 protein function was restored) and wild type group (after STK11 protein function was restored) in the dataset GSE72094. (**B**) Bubble diagram of biological processes (BP) enriched by down-regulated genes in the STK11 mutant group. Apoptosis and autophagy were highlighted with red boxes. (**C**) Mechanistic map of ICD caused by restoration of STK11 expression. (**D**) Fluorescent images of autophagy in A549 and LLC ^{KO} cells co-transfected with PBS, pSTK11, STK11@PP, and STK11@PPCM combined Lentivirus (mRFP-EGFP-Pruo) CMV-LC3B. Scale bar, 25 μm. (**E**) Western blotting analysis of STK11, light chain 3-I (LC3-I), light chain 3-II (LC3-II), and p62 expression in A549 and LLC ^{KO} cells after indicated treatments for 48 h. (**F** and **G**) Flow cytometry analysis of apoptosis on A549 and LLC ^{KO} cells after treatment with PBS, pSTK11, STK11@PP, and STK11@PPCM for 48 h. (**H**) CRT expression on A549 and LLC ^{KO} cells after indicated treatments for 48 h. Scale bar, 20 μm. (**I**) HMGB1 release on A549 and LLC ^{KO} cells after the indicated treatments for 48 h was evaluated by ELISA. (**J**) ATP release on A549 and LLC ^{KO} cells after the indicated treatments for 48 h was evaluated by ATP content assay kit (chemiluminescence). The data represented means ± SD ($n = 3$) and analyzed by a one-way ANOVA with a Tukey post-hoc test. Statistical significance: $^{*}P < 0.05$, $^{***}P < 0.001$, $^{****}P < 0.0001$ versus Ctrl

Figs. S24-S25). In addition, CD3 + CD8 + T cells and CD8 + effector T cells (IFN-γ+ T-bet+) in the treatment group were also increased compared to the saline-treated group (Figs. 5E, I and Figs. S24, S26). At the same time, M1 macrophage (CD86 + F4/80+) demonstrated the same trend within the tumor (Fig. 5K and Figs. S27-S28). STK11-mutated tumors have more exhausted T cells in the microenvironment, which leads to suppression of effective immune response and ineffective immune therapy [15, 55]. STK11@PPCM significantly reduced single-exhausted CD8 + T cells (CD8 + PD1+) and double-exhausted CD8 + T cells (Tim3 + PD1+) within tumors, compared to the control group (Fig. 5J and Fig. S26).

Moreover, Treg and M2 macrophages played important roles in tumor immune evasion, and their accumulation at the tumor site produced an ITME [56]. Flow cytometry results revealed that STK11@PPCM decreased the frequency of Treg (Foxp3 + CD4+) and M2 macrophage (CD206 + F4/80+) (Figs. 5D, H and Figs. S25, S28), indicating that STK11@PPCM reversed the ITME. Further evidence that STK11@PPCM triggered a robust anti-tumor immune response and reversed the ITME was demonstrated by the assessment of cytokine release. STK11@PPCM can increase the release of proinflammatory factors, including TNF-α, IL-6, and INF-γ, and decrease the release of anti-inflammatory factors, including TGF-β (Figs. 5L-O).

STK11@PPCM enhanced the anti-tumor efficacy of αPD1 in a mouse model of STK11-mutated lung adenocarcinoma

Previous findings indicated that STK11 mutation inhibited the efficacy of ICIs by creating a "cold" immune microenvironment, resulting in a poor prognosis in patients with LUAD [7–12]. In addition, we have demonstrated that STK11@PPCM was able to reverse the ITME and enhance the anti-tumor immune response. Based on these observations, we further explored whether the restoration of STK11 function could improve the anti-tumor efficacy of αPD1 in a LUAD model with STK11 mutation. Firstly, we constructed a subcutaneous LLC ^{KO} tumor model and were treated as indicated, which was the same as in Sect. 2.7 (Fig. 6A). The tumor growth rate was significantly inhibited in the STK11@PPCM + αPD1 group after three cycles of treatment, compared to STK11@PPCM or αPD1 alone, which demonstrated the strong anti-tumor efficacy of the combination therapy (Figs. 6B-D). The combination group significantly also prolonged the overall survival time of mice compared to other monotherapy groups (Fig. 6E), which was attributed to the strong and persistent immune activation induced by STK11@PPCM. At the same time, the combination of STK11@PPCM and αPD1 did not lead to a decrease in the body weight of mice (Fig. S29).

The in vitro experiments have demonstrated that restoration of STK11 function could activate autophagy and apoptotic processes, which caused the release of DAMPs and, in turn, triggered ICD. To explore the potential mechanisms in which combination therapy improved therapeutic efficacy, we performed autophagy, apoptosis, and ICD assays on tumor tissues. Firstly, immunofluorescence staining for STK11 and LC3 was performed, and the results indicated STK11 restoration and autophagy induction after combination treatment (Fig. 6F and Fig. S30). Besides, the tumor treated with STK11@PPCM + αPD1 exhibited the most remarkable apoptosis by hematoxylin and eosin (H&E) staining and TUNEL analyses (Fig. 6G and Fig. S31). Next, we examined molecular markers of ICD and found that the combination therapy group significantly increased the release of ATP and HMGB1 as well as upregulated CRT expression (Figs. 6F, H-I, and Fig. S30). In addition, it was noted that tumor-infiltrating CD8 + T cells were significantly increased in the combination therapy group compared to the other monotherapy groups, which was consistent with the previous flow assay results (Fig. 6F and Fig. S30).

Meanwhile, we exploratively demonstrated that STK11@PPCM was able to upregulate the expression of STING and PD-L1 in vivo by immunohistochemistry staining (IHC), consistent with the results of the in vitro assay (Fig. S32). In practice, treatment-related adverse effects were not negligible, and finally, we evaluated the side effects of combination therapy by hematology and histopathology in C57BL/6 mice. Mouse blood and major organs (i.e., heart, liver, spleen, lung, and kidney) were collected on day 25. We analyzed alanine

aminotransferase (ALT), aspartate aminotransferase (AST), total bilirubin (TBIL) and albumin (ALB) to assess liver function, and urea nitrogen (BUN) and creatinine (CR) to monitor kidney activity. We also performed routine blood tests to assess hematologic toxicity. These parameters were in the normal range after treatment with STK11@PPCM + αPD1 (Table S2 and Fig. S33). The results of H&E staining for major organs also showed no obvious histological differences between the combination and others (Fig. S34).

Discussion

The emergence of ICIs, such as anti-CTLA-4 and anti-PD-1/PD-L1 has become a first-line treatment option for advanced non-small cell lung cancer, greatly improving patient prognosis and changing the landscape of NSCLC treatment [2]. Unfortunately, less than 30% of patients with NSCLC benefit from ICIs, and 20–44% of lung cancer patients develop primary or secondary resistance to ICIs during treatment, which can be attributed to an inadequate tumor immunogenic and ITME [3]. Currently, to improve the immunogenicity of tumors, some measures have been taken to combine ICIs with chemotherapy, radiotherapy, or photodynamic therapy (PDT), which can trigger the immunogenic death of tumor cells, enhance cellular immunogenicity, and thus activate the anti-tumor immune response [57, 58]. However, radiotherapy and chemotherapy have serious toxic side effects, and PDT is ineffective in treating deep-seated tumors attributed to limited killing depth and range. Therefore, there is still a need to identify potential factors affecting the efficacy of immunotherapy and to explore a new safe, and effective strategy to enhance anti-tumor immune response and the sensitivity of tumor cells to ICIs.

STK11, a tumor suppressor gene, is involved in the occurrence and development of tumors. Recently, several clinical and preclinical studies have demonstrated that STK11 mutation is associated with poor prognosis in NSCLC treated with ICIs and is an important cause of resistance to ICIs, which was attributed to the shaping of an ITME by STK11 mutation [7–11]. STK11 is a key regulator of the LKB1-AMPK-mTOR signaling pathway, regulating autophagy and apoptosis, while STK11 mutation tends to result in down-regulation of apoptosis and autophagy processes [20, 21]. Autophagy is a tightly regulated pathway that not only has an important role in the regulation of basic metabolic functions, allowing cells to remove damaged or harmful components through catabolism and recycling to maintain a dynamic balance of nutrients and energy but also plays an important role in immune activation [59, 60]. Induction of autophagy and apoptosis in cancer cells could also promote the secretion of DAMPs, and the latter triggers ICD and enhances anti-tumor immunity response. Currently, there is a lack of effective treatment for lung cancer with STK11 mutation. Some small molecule antibodies or drugs, such as metformin [25, 26], PD-1/PD-L1 inhibitors in combination with chemotherapy and/or CTLA-4 inhibitors [27], inhibitors of STAT3 [10], and so on, have been taken to treat the STK11-deficient NSCLC. These regimens have been shown to produce some therapeutic activity in STK11 mutant lung cancer; however, these treatments demonstrated more severe toxicity and did not durably activate anti-tumor immunity. These features limited their practical application, which prompted us to further explore new therapies to enhance the durable anti-tumor immune response in STK11 mutant lung cancer. Deeply inspired by the COVID-19 nucleic acid vaccine, we speculated whether we could enhance anti-tumor immunity by restoring STK11 protein expression through gene therapy in STK11-mutant NSCLC.

It is known that nucleic acids such as DNA, mRNA, siRNA, or miRNA have been widely explored to modulate protein expression. Likewise, the mechanism of action and high specificity of these nucleic acids could present a possible therapy program for various cancers, compared to conventional drugs [29, 30]. Given the advantages of synthetic DNA for protein replacement, the use of synthetic DNA might restore the functions of STK11 without inducing substantial toxicity. Nucleic acids are easily degraded in the body and cannot be administered directly. With the rise of nanomaterials and the emergence of cationic polymers, such as PBAE, polyethyleneimine (PEI), cationic lipids, etc., they provide a powerful solution to this challenge. So, there is enough reason to believe that the STK11 protein function can be reactivated by nucleic acid nanoplatform based on STK11. So far, it has not been reported whether restoration of STK11 protein expression in STK11-mutated cells could reverse the ITME and enhance antitumor immunity.

Here, we constructed a new nucleic acid delivery platform (STK11@PPCM) composed of cationic polymers PBAE with the ability to complex the plasmid encoding STK11 and a layer of tumor cell membrane with the capability of actively targeting tumor lesions. We found that the STK11 plasmid DNA delivery platform effectively restored STK11 expression and could reactivate autophagy and apoptosis processes and cause the release of DAMPs, which further triggered ICD. Meanwhile, we found firstly that restoration of STK11 protein function effectively reversed the ITME by promoting DCs maturation, increasing tumor infiltration of CD8 + T cells and M1 macrophages, decreasing infiltration of Treg and M2 macrophages and increasing the expression of proinflammatory factors, such as TNF-α, IFN-γ and IL-6. Furthermore, the delivery platform showed notable therapeutic effects and safety in STK11-mutated

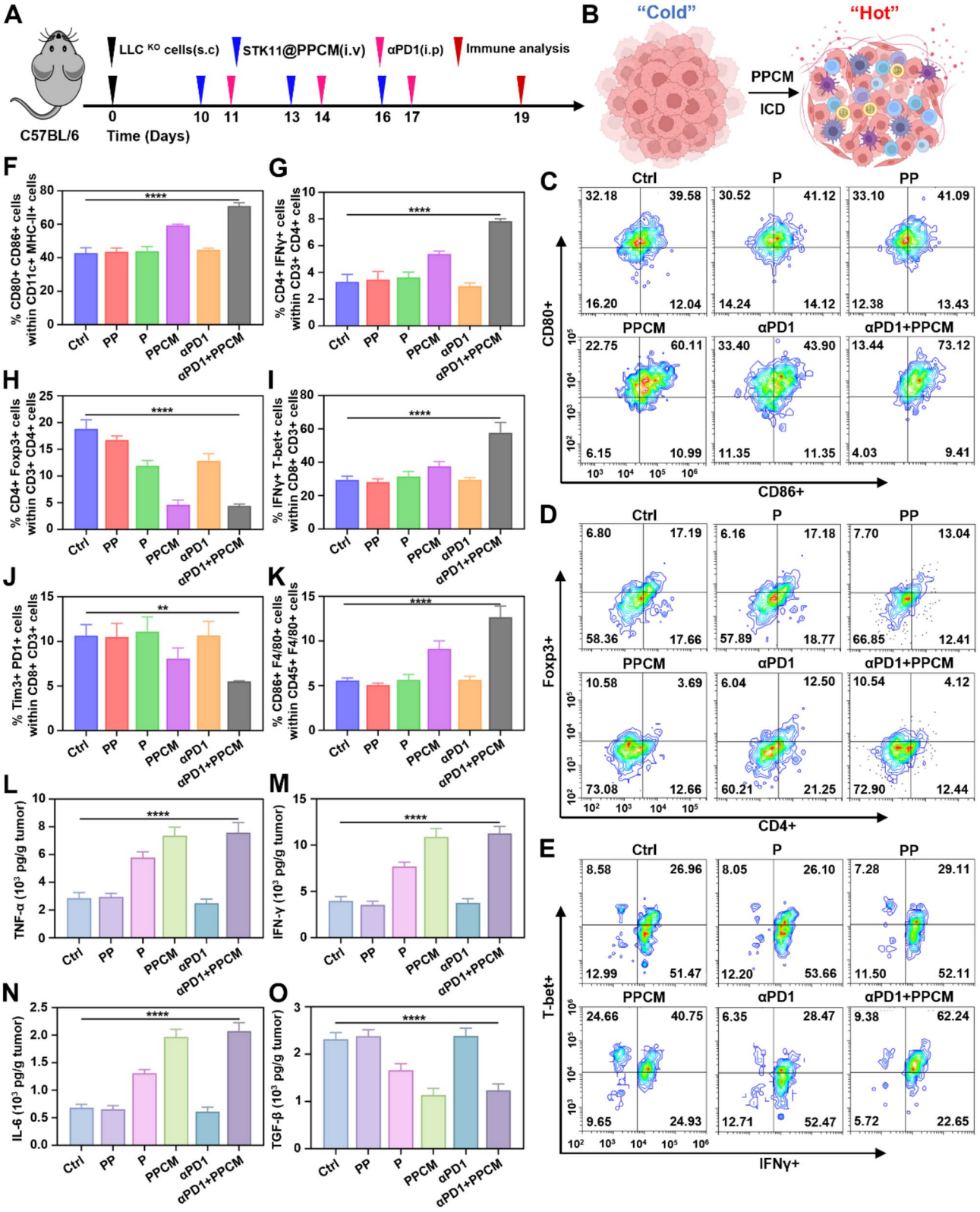

Fig. 5 (See legend on next page.)

(See figure on previous page.)

Fig. 5 STK11@PPCM reversed the "cold" immune microenvironment in the LLC ^{KO} tumor-bearing mouse model. (**A**) Experimental timeline for treatment of LLC ^{KO} tumor-bearing mice. S.C, subcutaneous; i.v, intravenous; i.p, intraperitoneal. (**B**) Schematic illustration of the reversed immune microenvironment in vivo. (**C**-**E**) The mapping of flow cytometry analysis of CD80 + CD86 + DCs (**C**) from lymph nodes, and CD4 + Foxp3 + T cells (**D**) and IFNγ + T-bet + T cells (**E**) from different treated tumors. (**F**-**K**) Flow cytometry analysis results of the percentage of CD80 + CD86 + DCs (**F**), and the percentage of CD4 + IFNγ + T cells (**G**), CD4 + Foxp3 + T cells (**H**), IFNγ + T-bet + T cells (**I**), Tim3 + PD1 + T cells (**J**) and CD86 + F4/80 + macrophage (**K**) from the tumors. Data are presented as means ± SD ($n = 3$ mice per group). (**L**-**O**) Results of ELISA analysis of cytokines in tumor tissue grinding fluid, including TNF-α (**L**), IFNγ (**M**), IL-6 (**N**), and TGF-β (**O**). Data are presented as means ± SD ($n = 3$ mice per group). Statistical significance was calculated via one-way ANOVA with a Tukey post hoc test. $^{**}P < 0.01$, $^{***}P < 0.001$ and $^{****}P < 0.0001$

tumor models treated with STK11@PPCM combined with αPD1. These results suggested that restoration of anti-oncogene function through DNA nanocomplexes can enhance the sensitivity of cancer cells to ICIs, providing a potential combination therapy strategy for other malignancies.

It is worth noting that this study has some limitations. For DNA delivery, DNA must be internalized into the nucleus and translated into a protein antigenic product, which decreases the effectiveness of the drug. Although our tumor-homologous cell membrane-mimicking nanoplatform was largely capable of targeting gene delivery to tumor sites, the risk of fusion of exogenous DNA with an organism's nuclear DNA cannot be ignored. Then, it should be noted that this study is limited to the STK11 tumor suppressor and it is not clear whether restoration of other tumor suppressors might have similar effects. In addition, only the C57BL/6 mouse homologous cellular LLC was investigated, and further validation may be needed in the future in humanized mice, organoids, or patient-derived tumor xenograft (PDX) models. At last, whether restoring STK11 expression in STK11 knockout mice can inhibit tumorigenesis also deserves to be further investigated, which would provide a theoretical basis for an STK11 nucleic acid vaccine.

In summary, our study provides a promising strategy for enhancing antitumor immune response, which may be beneficial to other malignant tumors bearing STK11 mutation. And, we expect the combination of STK11 nanomedicine with ICIs could provide a survival benefit to lung cancer patients with STK11 mutation in the future.

Materials and methods

Synthesis and purity identification of PBAE

PBAE cationic polymers were synthesized by a simple two-step strategy. First, 2.56 g of 1,4-butanediol diacrylate and 1.0 g of 4-amino-1-butanol were mixed in a glass bottle and then heated to 90 ℃ while stirring continuously for 24 h in Magnetic Stirrers under the condition of avoiding light. Second, 2.30 g of the reacted polymer was dissolved in 2 ml tetrahydrofuran, then added to 13 ml tetrahydrofuran dissolved with 786 mg of 1-(3-aminopropyl)-4-methylpiperazine. The resulting solution was stirred at room temperature for 2 h with 800 r/min. Subsequently, the obtained product was dissolved in diethyl ether, which was placed for 30 min. The ether was volatilized and the polymer powder was collected. Repeat the above process twice to get the purified substance. Last, the collected polymer was dried in a vacuum. After 48 h, the obtained polymer was dissolved in DMSO to a concentration of 100 mg/ml and stored at -20 ℃. According to the requirements of in vivo and in vitro experiments, we identified the purity of the synthesized PBAE cationic polymer by ^{1}H NMR spectra on an NMR spectrometer. The chemical shift (δ) was expressed as ppm, tetramethylsilane (TMS) was used as the internal standard, and DMSO-d was used as the solvent.

Preparation of PBAE/plasmid DNA nanocomplex (PP)

The prepared PBAE storage solution and DNA storage solution were dissolved respectively in sodium acetate buffer (25 mM, PH = 5.0) and incubated for 3 min at room temperature, followed by adding an equal volume of the polymer solution to the DNA solution and mixing well to ensure that the mass ratio (w/w) of PBAE/DNA was 90. The mixture was incubated at room temperature for 20 min, and the polymer molecules and DNA could combine and self-assemble to form PBAE/plasmid nanoparticles.

Preparation of PBAE/plasmid DNA/cell membrane (PPCM)

The PPCM was prepared by co-extrusion and sonication in an ice-water bath. The cell membrane solution extracted from tumor cells was thoroughly mixed with the PP complex and incubated at room temperature for 5 min, followed by ultrasound for 20 min (70 W, 40 kHz). After, the PPCM was obtained after extrusion of mixture mentioned above with 200 nm and 100 nm filter membranes for 10 times by extrusion apparatus. The PPCM solution was stored at 4 °C.

Cell culture and transfection

The cells used in the experiment were cultured in Dulbecco's Modified Eagle Medium (DMEM) with high glucose, supplemented with 10% fetal bovine serum and 1% penicillin-streptomycin solution, and cultured at 37 ℃ with 5% CO2. The 2×10^5 tumor cells were cultured in 6-well plates for 24 h before transfection, followed by the incubation with PBS, P, PP, and PPCM in fresh culture medium without FBS. After incubation for 6 h at 37 ℃ with 5% CO2, the culture medium was replaced with

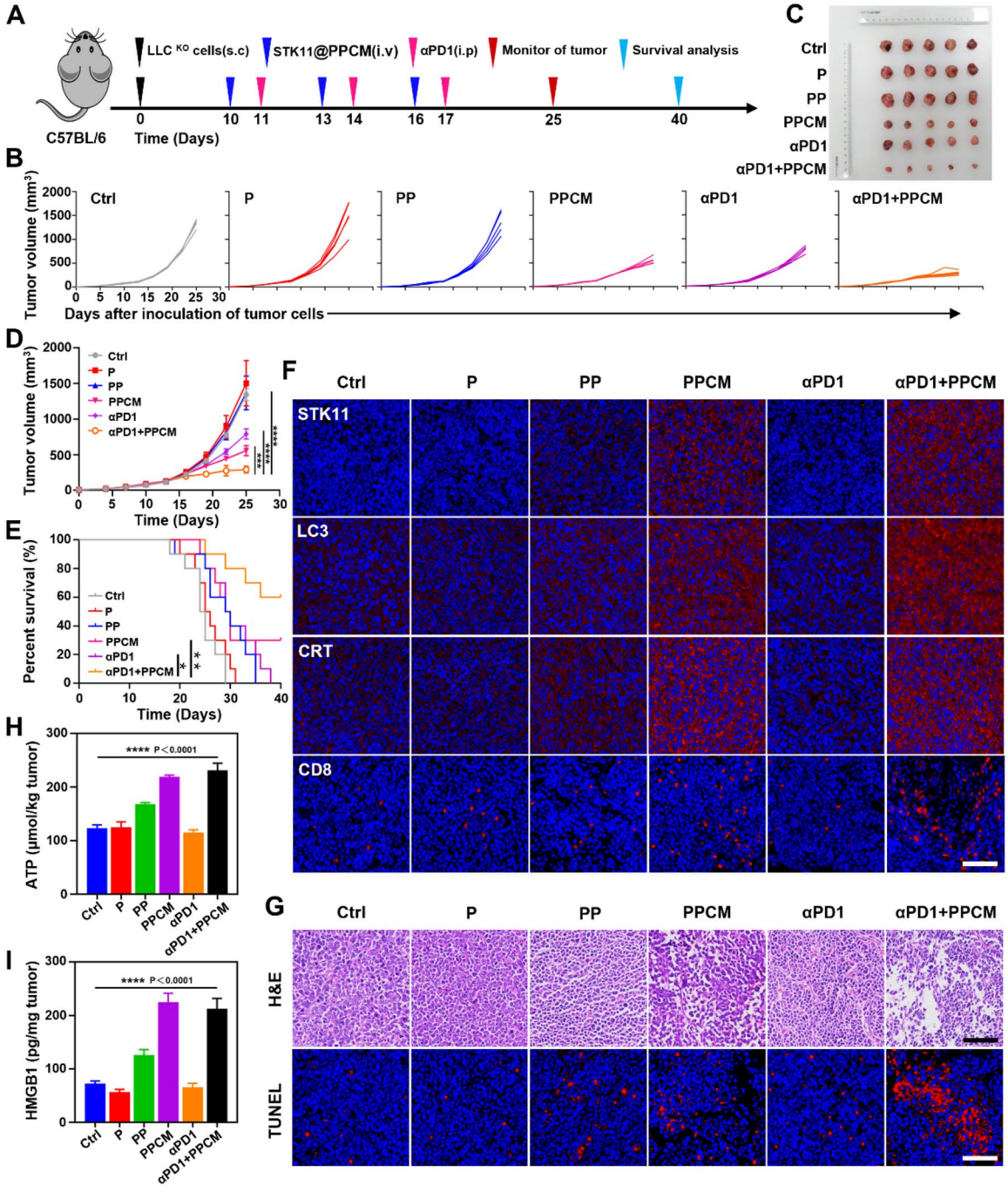

Fig. 6 STK11@PPCM increased the therapeutic efficacy of αPD1 in the STK11- mutated LLC tumor-bearing mouse model. (**A**) Experimental timeline for treatment of LLC ^{KO} tumor-bearing mice. S.C, subcutaneous; i.v, intravenous; i.p, intraperitoneal. (**B**) Individual tumor growth curves for mice treated as indicated. (**C**) Photographs of tumors excised from mice after different therapies on the 25th day. (**D**) The average tumor growth curves for mice treated as indicated. Data are represented as means ± SD ($n = 5$ mice per group). (**E**) The survival curve of mice after three rounds of treatment. (**F**) Immunofluorescence imaging from STK11-mutated LLC tumor tissues showed the expression of STK11(red), LC3 (red) and CRT (red), and CD8 + T cell infiltration (red) after treatment with saline, STK11 plasmid DNA, STK11@PP, STK11@PPCM, αPD1, or αPD1 + STK11@PPCM. Scale bars, 100 μm. (**G**) The H&E and TUNEL staining of tumor slices after receiving different treatments as indicated on the 25th day. The red color indicated apoptotic cells. Scale bar: 100 μm. (**H**) ATP levels in the supernatant of tumors excised from mice treated as indicated. Data are presented as means ± SD ($n = 3$ mice per group). (**I**) ELISA analysis of HMGB1 in the supernatant of tumors excised from mice treated as indicated. Data are presented as means ± SD ($n = 3$ mice per group). Statistical significance was calculated via one-way ANOVA with a Tukey post hoc test. $^{*}P < 0.05$, $^{**}P < 0.01$, $^{***}P < 0.001$ and $^{****}P < 0.0001$

fresh complete medium containing 10% FBS. After 48 h, the transfection efficiency was investigated by fluorescence microscope and flow cytometry (FCM).

Cellular uptake mechanism of PPCM in tumor cells

The cells were pre-incubated with different inhibitors, including promethazine (an inhibitor of clathrin-mediated endocytosis; 10 μg/ml), β-cyclodextrin (β-CD, an inhibitor of caveolae-mediated endocytosis; 5 mM) and amiloride (an inhibitor of micropinocytosis; 133 μg/ml), for 2 h at 37 °C before nanoparticles were added. The cells were also incubated at 37 °C without any inhibitors. After 2 h, the STK11 DNA, STK11@PP, and STK11@PPCM where plasmid DNA was labeled by Cy5 (red fluorescence) were separately added to the above pretreated cells and continued to be incubated at 37 °C for 6 h. Last, the fluorescence intensity was quantified using the FCM and confocal microscope (CLSM).

Western blot (WB)

Tumor cells were first seeded in a 6-well plate at a density of 2×10^5 cells per well. When the cells had grown to 70–80%, they were treated with PBS, naked DNA, PP, and PPCM for 48 h and then collected in a 2 ml clean centrifuge tube and resuspended with 100 μl of RIPA containing 1% PMSF on the ice. After 30 min, the protein concentration was tested by BCA assay. 40 μg of protein per well was separated by 4–20% gradient preformed adhesive (160 V, 50 min) and transferred onto PVDF membranes using a wet-transfer system (300 mA, 1 h). Next, the PVDF membrane was sealed with a rapid sealing solution for 10 min and then incubated overnight with appropriate primary antibodies at 4 °C. Afterward, the PVDF membrane was washed with TBST three times and incubated with proper secondary antibodies at room temperature for 2 h. Last, the PVDF membrane was developed by an ultrasensitive ECL chemiluminescence kit.

Quantitative Real-time PCR (qRT-PCR) assay

When cells were treated with PBS, naked DNA, PP, and PPCM for 48 h, total RNA from tumor cells was extracted by Trizol and then reverse-transcribed into cDNA using the HiScript® II Q RT SuperMix for qPCR (+ gDNA wiper), according to the manufacturer's instructions. RT-PCR was conducted to measure mRNA using the SYBR Green Master Mix, and GAPDH or β-actin was selected as an internal reference gene. Primers used in the experiment were designed according to the NCBI database. All primers were listed in Table S3.

In vitro toxicity and apoptosis assessment induced by STK11 nanocomplex

A549 and LLC ^{KO} cells were seeded separately in 96-well plates at a density of 1×10^4 cells/well and incubated with 100 μl of complete medium for 24 h. When the cells had grown to 70–80%, the cells were treated with PBS, naked STK11 DNA, STK11@PP, and STK11@PPCM for 48 h. The absorbance was measured at a wavelength of 450 nm using a microplate reader.

Apoptosis was also tested using Annexin V-FITC Apoptosis Detection Kit and One Step TUNEL Apoptosis Assay Kit by flow cytometry and inverted fluorescence microscope. In short, the cells seeded in 6-well plates were treated for 48 h. Subsequently, the treated cells were collected or fixed for flow detection or fluorescence imaging, according to the manufacturer's instructions.

In vitro autophagy detection by lentivirus (mRFP-EGFP-Pruo) CMV-LC3B

Autophagy induced by STK11 nanocomplex was detected using Lentivirus (mRFP-EGFP-Pruo) CMV-LC3B by inverted fluorescence microscope. First, A549 and LLC ^{KO} cells were seeded separately in 6-well plates for 24 h before transfection, followed by the incubation with PBS, naked STK11 DNA, STK11@PP, and STK11@PPCM in fresh culture medium without FBS. After 6 h, the culture medium was replaced with fresh medium containing 10% FBS and Lentivirus (mRFP-EGFP-Pruo) CMV-LC3B (A549: MOI = 200, LLC ^{KO}: MOI = 300) and incubated for 24 h. Subsequently, the virus-containing medium was replaced with fresh virus-free complete medium and the cells continued to be cultured for 24 h. At last, autophagic flux was observed under fluorescence microscopy.

Cell Immunofluorescence staining (IF)

A549 and LLC ^{KO} cells were seeded separately into confocal dishes at a density of 1×10^5 cells/dish and incubated with 1 ml of complete medium for 24 h. When the cells had grown to 70–80%, the cells were treated with PBS, naked STK11 DNA, STK11@PP, and STK11@PPCM for 48 h. Then, the cells were washed with PBS and fixed with 4% paraformaldehyde for 15 min at room temperature. Next, the cells were permeabilized with 0.5% Triton X-100 for 20 min and blocked with concentrated normal goat serum for 30 min at room temperature. Soon after, the samples were incubated overnight with calreticulin Polyclonal antibody (CRT) at 4 °C. Afterward, the samples were washed with PBS three times and incubated with Cy3-AffiniPure Goat Anti-Rabbit lgG (H + L) in the wet box at 37° for 1 h. After that, the samples were stained with DAPI for 10 min under low light conditions. At last, they were washed with PBS three times and imaged using confocal microscopy.

ATP, HMGB1, and cytokine assays

To confirm that restoration of STK11 expression triggered immunogenic death, ATP and HMGB1 released by A549 and LLC ^{KO} cells were assayed by the ATP content assay kit (chemiluminescence) and Human or Mouse HMGB1 ELISA Kit. The cells were first seeded in a 6-well plate and incubated for 24 h. Then, the old medium was replaced by fresh complete medium containing PBS, naked STK11 DNA, STK11@PP, or STK11@PPCM, and the cells were incubated for 48 h. Last, the cell culture supernatant was collected by centrifugation at 3000 rpm for 10 min and tested by kits, according to the manufacturer's instructions.

For evaluation of ATP, HMGB1, and cytokines within the tumor, such as TNF-α, IFN-γ, IL-6, and TNF-β, tumor tissue was collected and ground. The supernatant from the tumor grinding solution was then detected with ELISA kits, according to the synopsis.

Flow cytometry assay for immune cells in tissues

All antibodies for flow assay were purchased from Elabscience and BioLegend and listed in Table S4. The tumors and lymph nodes were free and cut into small pieces using sterile ophthalmic scissors, and then, these small pieces were washed repeatedly with sterile PBS and ground using a syringe. The grinding solution was then passed through a 70-μm mesh nylon cell strainer to form single-cell suspensions. For the flow assay of cell surface markers, flow cytometry antibodies (5ul/Test) were added to the cell suspension and incubated at 4℃ for 30 min under light protection, according to the manufacturer's instructions. For the staining of intracellular markers, such as IFN-γ, Foxp3, and T-bet, the cells were fixed and permeabilized at 4 °C for 30 min, and then, stained with appropriate antibodies at 4 °C for 30 min. Last, the stained cells were tested by flow cytometry and analyzed using FlowJo software.

Immunofluorescence staining and TUNEL assay in tissues

To confirm that restorative STK11 expression triggered immunogenic death, autophagy, and apoptosis, STK11, LC3, and CRT in tumors were tested by immunofluorescence staining, and then, apoptosis was tested in tissue using the TUNEL Kit. Briefly, tissue sections were deparaffinized with xylene and rehydrated with ethanol, then cell and nuclear membranes were permeabilized with proteinase K. For immunofluorescence staining, samples were incubated with different primary rabbit antibodies at a 1:50 dilution overnight at 4 °C, washed with PBS, and incubated with fluorescently labeled secondary antibodies (1:1000) for one hour at room temperature. For the TUNEL assay, sections were washed in PBS and incubated with reaction solution for 1 h at 37 °C in a humidified atmosphere in the dark, according to the manufacturer's instructions. Last, the slides were imaged using an inverted fluorescence microscope.

Assessment of the immune microenvironment and antitumor immune efficacy induced by STK11@PPCM in LLC ^{KO}-bearing tumor mouse model

To confirm that restoration of STK11 expression reversed the immunosuppressive microenvironment and enhanced the efficacy of ICIs, 1×10^6 LLC ^{KO} cells per mouse were inoculated subcutaneously in the right axilla of the right forelimb of C57BL/6 mice to establish a subcutaneous graft tumor model. When the tumor volume reached 60–80 mm^3, the tumor-bearing mice were randomly divided into 6 groups ($n = 10$ mice per group, 5 mice were used for efficacy assessment, 5 mice were used for immune microenvironment assessment), which received respectively 100 μl of saline, naked STK11 plasmid, STK11@PP, STK11@PPCM, anti-PD-1, or STK11@PPCM + anti-PD-1 via tail vein at a DNA dose of 25 μg per mice at days 10, 13, and 16 after tumor implantation. Two groups of mice receiving anti-PD-1 were treated with intraperitoneal administration of anti-PD-1 (100 μg in 100 μl saline per mouse) on days 11, 14, and 17. At day 19, 5 mice in each group were euthanized and the tumors and groin lymph nodes were isolated to examine the immune cells. The number and phenotype of immune cells, such as T cells, DCs, and macrophages, and the concentration of secreted cytokines were detected by flow cytometry and ELISA Kits. An additional 5 mice in each group were used to assess therapeutic efficacy and tumor sizes were measured every 3 days after tumor implantation, and the average tumor volume was calculated according to the following formula: length × width × width/2. At the same time, the body weight of the 5 mice assessed therapeutic efficacy was recorded every 3 days after tumor implantation. On day 25, the 5 mice were euthanized and the tumors were isolated to image.

Statistical analysis

All experiments were repeated 3 times and all results are presented as the means ± SD. A Student's t-test or Mann-Whitney test was used for two-group comparisons, and a one-way analysis of variance (ANOVA) was used to compare more than two groups. Survival curves were compared by the Log-Rank test. All statistical analyses were carried out using GraphPad Prism 7 software and R Studio 4.2.2, and statistical significance was indicated as $^*P < 0.05$, $^{**}P < 0.01$, $^{***}P < 0.001$, and $^{****}P < 0.0001$, and ns indicated no significant difference.

Abbreviations

STK11	Serine/Threonine Kinase 11
ITME	Immunosuppressive Tumor Microenvironment
ICIs	Immune Checkpoint Inhibitors
NSCLC	Non-Small Cell Lung Cancer

DAMPs	Damage Associated Molecular Patterns
αPD1	Anti-PD-1
PD-1	Programmed Cell Death-1
PD-L1	Programmed cell Death-Ligand 1
AMPK	Adenosine Monophosphate-activated Protein Kinase
STING	Stimulator of Interferon Genes
ICD	Immunogenic Cell Death
HMGB1	High-Mobility Group Box 1
CRT	Calreticulin
CTLA-4	Cytotoxic T Lymphocyte-associated Antigen-4
siRNA	Small Interfering RNA
PBAE	Poly (β-Amino Ester)
pcDNA	Plasmid DNA
ALT	Alanine Aminotransferase
AST	Aspartate Aminotransferase
TBIL	Total Bilirubin
ALB	Albumin
BUN	Urea Nitrogen
CR	Creatinine

Supplementary Information

The online version contains supplementary material available at https://doi.org/10.1186/s12951-025-03404-z.

Supplementary Material 1

Supplementary Material 2

Acknowledgements
We were very grateful for the support of the public research platform of Zhongda Hospital, Southeast University for the flow cytometry.

Author contributions
Z.S. and Q.W. designed the study, performed the experiments, and drafted the manuscript. H.X. and J.X. integrated the data and manuscript revision. Z.Z., L.Q. and Y.T. participated in the experiments. Q.S. and T.L. reviewed the manuscript. X.L., H.J., S.H. and X.W. were responsible for the study concept and supervision. All authors have read and approved the article.

Funding
This work was supported by the National Natural Science Foundation of China (82061148012, 82027806, 82372220); Beijing Medical Award Foundation (YXJX-2022-0435-0372); Wu Jieping Medical Foundation (320.6750.2023-17-3).

Data availability
No datasets were generated or analysed during the current study.

Declarations

Ethics approval and consent to participate
All the animal experiments were approved by the Ethics Committee of Southeast University School of Medicine (Approval number: **20230308007**). The sample collection and the use of the corresponding clinical data of patients were approved by the Ethics Committee of Zhongda Hospital, Southeast University (Approval number: **2023ZDSYLL212-P01**). All the authors complied with all relevant ethical regulations.

Consent for publication
All authors agree to be published.

Competing interests
The authors declare no competing interests.

Author details
[1]Department of Pulmonary and Critical Care Medicine, Medical School, Zhongda Hospital, Southeast University, Nanjing, Jiangsu 210009, China
[2]Health Management Center, Weifang People's Hospital, Shandong Second Medical University, Weifang, Shandong 261000, China
[3]State Key Laboratory of Digital Medical Engineering, National Demonstration Center for Experimental Biomedical Engineering Education, School of Biological Science and Medical Engineering, Southeast University, Nanjing, Jiangsu 210096, China

Received: 21 November 2024 / Accepted: 15 April 2025
Published online: 24 April 2025

References

1. Filho AM, Laversanne M, Ferlay J, Colombet M, Piñeros M, Znaor A, et al. The GLOBOCAN 2022 cancer estimates: data sources, methods, and a snapshot of the cancer burden worldwide. Int J Cancer. 2025;156:1336–46.
2. Riely GJ, Wood DE, Ettinger DS, Aisner DL, Akerley W, Bauman JR, et al. Non-Small cell lung cancer, version 4.2024, NCCN clinical practice guidelines in oncology. J Natl Compr Canc Netw. 2024;22:249–74.
3. Kalbasi A, Ribas A. Tumour-intrinsic resistance to immune checkpoint Blockade. Nat Rev Immunol. 2020;20:25–39.
4. Shackelford DB, Shaw RJ. The LKB1–AMPK pathway: metabolism and growth control in tumour suppression. Nat Rev Cancer. 2009;9:563–75.
5. Gillette MA, Satpathy S, Cao S, Dhanasekaran SM, Vasaikar SV, Krug K, et al. Proteogenomic characterization reveals therapeutic vulnerabilities in lung adenocarcinoma. Cell. 2020;182:200–e22535.
6. Farooq H, Bien H, Chang V, Becker D, Park Y-H, Bates SE. Loss of function STK11 alterations and poor outcomes in non–small-cell lung cancer: literature and case series of US veterans. Semin Oncol. 2022;49:319–25.
7. Yang Y, Wang Z, Fang J, Yu Q, Han B, Cang S, et al. Efficacy and safety of sintilimab plus pemetrexed and platinum as First-Line treatment for locally advanced or metastatic nonsquamous NSCLC: a randomized, Double-Blind, phase 3 study (Oncology pRogram by innovent anti-PD-1-11). J Thorac Oncol. 2020;15:1636–46.
8. Skoulidis F, Goldberg ME, Greenawalt DM, Hellmann MD, Awad MM, Gainor JF, et al. *STK11/LKB1* mutations and PD-1 inhibitor resistance in *KRAS* -Mutant lung adenocarcinoma. Cancer Discov. 2018;8:822–35.
9. Deng J, Thennavan A, Dolgalev I, Chen T, Li J, Marzio A, et al. ULK1 Inhibition overcomes compromised antigen presentation and restores antitumor immunity in LKB1-mutant lung cancer. Nat Cancer. 2021;2:503–14.
10. Pore N, Wu S, Standifer N, Jure-Kunkel M, De Los Reyes M, Shrestha Y, et al. Resistance to durvalumab and durvalumab plus Tremelimumab is associated with functional *STK11* mutations in patients with Non–Small cell lung Cancer and is reversed by STAT3 knockdown. Cancer Discov. 2021;11:2828–45.
11. Gao Y, Päivinen P, Tripathi S, Domènech-Moreno E, Wong IPL, Vaahtomeri K, et al. Inactivation of AMPK leads to Attenuation of antigen presentation and immune evasion in lung adenocarcinoma. Clin Cancer Res. 2022;28:227–37.
12. Goldschmid H, Kluck K, Ball M, Kirchner M, Allgäuer M, Winter H, et al. Spatial profiling of the microenvironment reveals low intratumoral heterogeneity and STK11-associated immune evasion in therapy-naïve lung adenocarcinomas. Lung Cancer. 2023;180:107212.
13. Kitajima S, Ivanova E, Guo S, Yoshida R, Campisi M, Sundararaman SK, et al. Suppression of STING associated with LKB1 loss in KRAS-Driven lung Cancer. Cancer Discov. 2019;9:34–45.
14. Li A, Wang Y, Yu Z, Tan Z, He L, Fu S, et al. STK11/LKB1-Deficient phenotype rather than mutation diminishes immunotherapy efficacy and represents STING/Type I Interferon/CD8 + T-Cell dysfunction in NSCLC. J Thorac Oncol. 2023;18:1714–30.
15. Qian Y, Galan-Cobo A, Guijarro I, Dang M, Molkentine D, Poteete A, et al. MCT4-dependent lactate secretion suppresses antitumor immunity in LKB1-deficient lung adenocarcinoma. Cancer Cell. 2023;41:1363–e13807.
16. Skoulidis F, Heymach JV. Co-occurring genomic alterations in non-small-cell lung cancer biology and therapy. Nat Rev Cancer. 2019;19:495–509.
17. Wani A, Al Rihani SB, Sharma A, Weadick B, Govindarajan R, Khan SU, et al. Crocetin promotes clearance of amyloid-β by inducing autophagy via the STK11/LKB1-mediated AMPK pathway. Autophagy. 2021;17:3813–32.
18. Chen X, Mao R, Su W, Yang X, Geng Q, Guo C, et al. Circular RNA circHIPK3 modulates autophagy via MIR124-3p-STAT3-PRKAA/AMPKα signaling in STK11 mutant lung cancer. Autophagy. 2020;16:659–71.
19. Muniraj N, Siddharth S, Shriver M, Nagalingam A, Parida S, Woo J, et al. Induction of STK11-dependent cytoprotective autophagy in breast cancer cells upon Honokiol treatment. Cell Death Discov. 2020;6:81.
20. Gao W, Wang X, Zhou Y, Wang X, Yu Y. Autophagy, ferroptosis, pyroptosis, and necroptosis in tumor immunotherapy. Sig Transduct Target Ther. 2022;7:1–26.

21. Catanzaro E, Beltrán-Visiedo M, Galluzzi L, Krysko DV. Immunogenicity of cell death and cancer immunotherapy with immune checkpoint inhibitors. Cell Mol Immunol. 2025;22:24–39.
22. Kroemer G, Galassi C, Zitvogel L, Galluzzi L. Immunogenic cell stress and death. Nat Immunol. 2022;23:487–500.
23. Fucikova J, Kepp O, Kasikova L, Petroni G, Yamazaki T, Liu P, et al. Detection of Immunogenic cell death and its relevance for cancer therapy. Cell Death Dis. 2020;11:1–13.
24. Li Z, Lai X, Fu S, Ren L, Cai H, Zhang H, et al. Immunogenic cell death activates the tumor immune microenvironment to boost the immunotherapy efficiency. Adv Sci (Weinh). 2022;9:e2201734.
25. Marrone KA, Zhou X, Forde PM, Purtell M, Brahmer JR, Hann CL, et al. A randomized phase II study of Metformin plus Paclitaxel/Carboplatin/Bevacizumab in patients with Chemotherapy-Naïve advanced or metastatic nonsquamous Non-Small cell lung Cancer. Oncologist. 2018;23:859–65.
26. Wang Z, Lu C, Zhang K, Lin C, Wu F, Tang X et al. Metformin combining PD-1 inhibitor enhanced Anti-Tumor efficacy in STK11 mutant lung Cancer through AXIN-1-Dependent Inhibition of STING ubiquitination. Front Mol Biosci. 2022;9.
27. Skoulidis F, Araujo HA, Do MT, Qian Y, Sun X, Cobo AG et al. CTLA4 Blockade abrogates KEAP1/STK11-related resistance to PD-(L)1 inhibitors. Nature. 2024;1–10.
28. Mendes BB, Conniot J, Avital A, Yao D, Jiang X, Zhou X, et al. Nanodelivery of nucleic acids. Nat Rev Methods Primers. 2022;2:1–21.
29. Dunbar CE, High KA, Joung JK, Kohn DB, Ozawa K, Sadelain M. Gene therapy comes of age. Science. 2018;359:eaan4672.
30. Huayamares SG, Loughrey D, Kim H, Dahlman JE, Sorscher EJ. Nucleic acid-based drugs for patients with solid tumours. Nat Rev Clin Oncol. 2024;21:407–27.
31. Liu Y, Li Y, Keskin D, Shi L. Poly(β-Amino Esters): Synthesis, Formulations, and Their Biomedical Applications. Adv Healthc Mater. 2019;8:1801359.
32. Zhang J, Cai X, Dou R, Guo C, Tang J, Hu Y, et al. Poly(β-amino ester)s-based nanovehicles: structural regulation and gene delivery. Mol Therapy - Nucleic Acids. 2023;32:568–81.
33. Keeney M, Ong S-G, Padilla A, Yao Z, Goodman S, Wu JC, et al. Development of Poly(β-amino ester)-Based biodegradable nanoparticles for nonviral delivery of minicircle DNA. ACS Nano. 2013;7:7241–50.
34. Wilson DR, Mosenia A, Suprenant MP, Upadhya R, Routkevitch D, Meyer RA, et al. Continuous microfluidic assembly of biodegradable poly(beta-amino ester)/DNA nanoparticles for enhanced gene delivery. J Biomedical Mater Res Part A. 2017;105:1813–25.
35. Oroojalian F, Beygi M, Baradaran B, Mokhtarzadeh A, Shahbazi M-A. Immune cell Membrane-Coated biomimetic nanoparticles for targeted Cancer therapy. Small. 2021;17:2006484.
36. Chen X, Liu B, Tong R, Zhan L, Yin X, Luo X, et al. Orchestration of biomimetic membrane coating and nanotherapeutics in personalized anticancer therapy. Biomater Sci. 2021;9:590–625.
37. Ren X, Yang S, Yu N, Sharjeel A, Jiang Q, Macharia DK, et al. Cell membrane camouflaged bismuth nanoparticles for targeted photothermal therapy of homotypic tumors. J Colloid Interface Sci. 2021;591:229–38.
38. Schabath MB, Welsh EA, Fulp WJ, Chen L, Teer JK, Thompson ZJ, et al. Differential association of STK11 and TP53 with KRAS mutation-associated gene expression, proliferation and immune surveillance in lung adenocarcinoma. Oncogene. 2016;35:3209–16.
39. Best SA, Gubser PM, Sethumadhavan S, Kersbergen A, Negrón Abril YL, Goldford J, et al. Glutaminase inhibition impairs CD8 T cell activation in *STK11-/Lkb1*-deficient lung cancer. Cell Metabol. 2022;34:874–e8876.
40. Rousseaux S, Debernardi A, Jacquiau B, Vitte A-L, Vesin A, Nagy-Mignotte H, et al. Ectopic activation of germline and placental genes identifies aggressive Metastasis-Prone lung cancers. Sci Transl Med. 2013;5:ra18666–18666.
41. Okayama H, Kohno T, Ishii Y, Shimada Y, Shiraishi K, Iwakawa R, et al. Identification of genes upregulated in ALK-Positive and EGFR/KRAS/ALK-Negative lung adenocarcinomas. Cancer Res. 2012;72:100–11.
42. Yamauchi M, Yamaguchi R, Nakata A, Kohno T, Nagasaki M, Shimamura T, et al. Epidermal growth factor receptor tyrosine kinase defines critical prognostic genes of stage I lung adenocarcinoma. PLoS ONE. 2012;7:e43923.
43. Foy J-P, Karabajakian A, Ortiz-Cuaran S, Boussageon M, Michon L, Bouaoud J, et al. Datasets for gene expression profiles of head and neck squamous cell carcinoma and lung cancer treated or not by PD1/PD-L1 inhibitors. Data Brief. 2022;44:108556.
44. Foy J-P, Karabajakian A, Ortiz-Cuaran S, Boussageon M, Michon L, Bouaoud J, et al. Immunologically active phenotype by gene expression profiling is associated with clinical benefit from PD-1/PD-L1 inhibitors in real-world head and neck and lung cancer patients. Eur J Cancer. 2022;174:287–98.
45. Jung H, Kim HS, Kim JY, Sun J-M, Ahn JS, Ahn M-J, et al. DNA methylation loss promotes immune evasion of tumours with high mutation and copy number load. Nat Commun. 2019;10:4278.
46. Kim JY, Choi JK, Jung H. Genome-wide methylation patterns predict clinical benefit of immunotherapy in lung cancer. Clin Epigenetics. 2020;12:119.
47. Patel AK, Kaczmarek JC, Bose S, Kauffman KJ, Mir F, Heartlein MW, et al. Inhaled nanoformulated mRNA polyplexes for protein production in lung epithelium. Adv Mater. 2019;31:1805116.
48. Liu S, Gao Y, Zhou D, Zeng M, Alshehri F, Newland B, et al. Highly branched poly(β-amino ester) delivery of minicircle DNA for transfection of neurodegenerative disease related cells. Nat Commun. 2019;10:3307.
49. Zhang L, Deng S, Zhang Y, Peng Q, Li H, Wang P, et al. Homotypic targeting delivery of SiRNA with artificial Cancer cells. Adv Healthc Mater. 2020;9:1900772.
50. Yan X, Pan Q, Xin H, Chen Y, Ping Y. Genome-editing prodrug: targeted delivery and conditional stabilization of CRISPR-Cas9 for precision therapy of inflammatory disease. Sci Adv. 2021;7:eabj0624.
51. Liu L, Bai X, Martikainen M-V, Kårlund A, Roponen M, Xu W, et al. Cell membrane coating integrity affects the internalization mechanism of biomimetic nanoparticles. Nat Commun. 2021;12:5726.
52. Han S, Lee Y, Lee M. Biomimetic cell membrane-coated DNA nanoparticles for gene delivery to glioblastoma. J Controlled Release. 2021;338:22–32.
53. Liu Y-T, Sun Z-J. Turning cold tumors into hot tumors by improving T-cell infiltration. Theranostics. 2021;11:5365–86.
54. Xiang X, Wang J, Lu D, Xu X. Targeting tumor-associated macrophages to synergize tumor immunotherapy. Sig Transduct Target Ther. 2021;6:1–12.
55. Riley RS, June CH, Langer R, Mitchell MJ. Delivery technologies for cancer immunotherapy. Nat Rev Drug Discov. 2019;18:175–96.
56. Feng S, Cheng X, Zhang L, Lu X, Chaudhary S, Teng R et al. Myeloid-derived suppressor cells inhibit T cell activation through nitrating LCK in mouse cancers. Proceedings of the National Academy of Sciences. 2018;115:10094–9.
57. Zhang Z, Liu X, Chen D, Yu J. Radiotherapy combined with immunotherapy: the dawn of cancer treatment. Sig Transduct Target Ther. 2022;7:1–34.
58. Zhang S, Wang J, Kong Z, Sun X, He Z, Sun B, et al. Emerging photodynamic nanotherapeutics for inducing Immunogenic cell death and potentiating cancer immunotherapy. Biomaterials. 2022;282:121433.
59. Xia H, Green DR, Zou W. Autophagy in tumour immunity and therapy. Nat Rev Cancer. 2021;21:281–97.
60. Niu X, You Q, Hou K, Tian Y, Wei P, Zhu Y, et al. Autophagy in cancer development, immune evasion, and drug resistance. Drug Resist Updat. 2025;78:101170.

Publisher's note